Nano-Micro Letters

e-ISSN 2150-5551
CN 31-2103/TB

ARTICLE

https://doi.org/10.1007/s40820-025-02010-w

Cite as
Nano-Micro Lett.
(2026) 18:157

Received: 18 August 2025
Accepted: 5 November 2025

Vertical Interfacial Engineering in Two-Step-Processed Perovskite Films Enabled by Dual-Interface Modification for High-Efficiency p-i-n Solar Cells

Wenhao Zhou[1], Heng Liu[2,3], Haiyan Li[4], Weihai Zhang[1,2] ✉, Hui Li[1], Xia Zhou[1], Rouxi Chen[5], Wenjun Zhang[1], Tingting Shi[4] ✉, Antonio Abate[1] ✉, Hsing-Lin Wang[2] ✉

HIGHLIGHTS

- A vertical interfacial engineering strategy via dual-interface modification ($Sn(OTF)_2$ at NiO_x/perovskite, 4-Fluorophenylethylamine chloride (F-PEA) at perovskite/C60) solves energy-level mismatches in two-step-processed (TSP) p-i-n PSCs, boosting PCE to 25.6%.
- $Sn(OTF)_2$ enhances NiO_x conductivity, suppresses ion migration, and forms a Pb-Sn perovskite interlayer; F-PEA eliminates PbI_2, forming a 2D capping layer for defect passivation.
- Optimized NiO_x-based TSP p-i-n PSCs retain 84% initial power conversion efficiency after 720-h light illumination, providing design principles for 26%-efficiency devices.

ABSTRACT Two-step-processed (TSP) inverted p-i-n perovskite solar cells (PSCs) have demonstrated significant promise in tandem applications. However, the power conversion efficiency (PCE) of TSP p-i-n PSCs rarely exceeds 24%. Here, we demonstrate that TSP perovskite films exhibit a vertically gradient distribution of residual PbI_2 clusters, which form Schottky heterojunctions with the perovskite, leading to substantial interfacial energy-level mismatches within NiO_x-based TSP p-i-n PSCs. These limitations were effectively addressed via a vertical interfacial engineering enabled by dual-interface modification incorporating tin trifluoromethanesulfonate ($Sn(OTF)_2$) and 4-Fluorophenylethylamine chloride (F-PEA) at the NiO_x/perovskite and perovskite/C60 interfaces, respectively. The functional $Sn(OTF)_2$ not only enhances the conductivity of NiO_x films but also suppresses ion migration, while inducing the formation of a Pb-Sn mixed perovskite interlayer that precisely regulates the energy level at the NiO_x/perovskite interface. Complementally, F-PEA post-treatment effectively converts surface residual PbI_2 clusters into a 2D perovskite capping layer, which simultaneously passivates surface defects and enhances energy-level alignment at the perovskite/C60 interface. Consequently, the optimized NiO_x-based TSP p-i-n PSCs achieve a notable PCE of 25.6% with superior operational stability. This study elucidates the underlying mechanisms limiting the efficiency of TSP p-i-n PSCs, while establishing design principles for these devices targeting 26% efficiency.

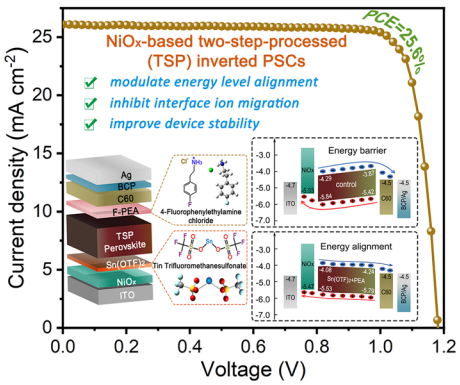

KEYWORDS Vertical interfacial engineering; Interface modification; Energy-level modulation; Nickle oxide; Two-step procession

Wenhao Zhou, Heng Liu, and Haiyan Li have contributed equally to this work.

✉ Weihai Zhang, zhangwh@nbut.edu.cn; Tingting Shi, ttshi@jnu.edu.cn; Antonio Abate, antonio.abate@unina.it; Hsing-Lin Wang, wangxl3@sustech.edu.cn

[1] School of New Energy, Ningbo University of Technology, Ningbo 315211, People's Republic of China
[2] Department of Materials Science and Engineering, Southern University of Science and Technology, Shenzhen 518055, People's Republic of China
[3] Institute of Materials, Henan Academy of Sciences, Zhengzhou 450046, People's Republic of China
[4] Siyuan Laboratory, Guangzhou Key Laboratory of Vacuum Coating Technologies and New Energy Materials, Department of Physics, Jinan University, Guangzhou 510632, People's Republic of China
[5] School of Innovation and Entrepreneurship, Southern University of Science and Technology, Shenzhen 518055, People's Republic of China

Published online: 05 January 2026

Shanghai Jiao Tong University Press

Springer

1 Introduction

Perovskite solar cells (PSCs) have garnered significant global research interest over the past decade owing to their exceptional advantages, including cost-effective fabrication, high device efficiency, and superior defect tolerance [1, 2]. Through innovations in material design and device engineering, the power conversion efficiency (PCE) of PSCs has reached certified record values of 27.0% in single-junction configurations and 34.6% in perovskite-silicon tandem architectures, positioning them as a leading candidate for next-generation photovoltaic technologies [3–5]. Among strategies for advancing PSCs, the inverted p-i-n architecture has attracted considerable attention due to its negligible hysteresis, low-temperature processability, high stability, and low parasitic absorption. Such features render this architecture particularly suitable for flexible devices and monolithic perovskite-silicon tandem solar cells.

Within p-i-n device architectures, perovskite films are typically deposited on a hole transport layer (HTL) such as poly(3,4-ethylenedioxythiophene)/polystyrene sulfonate (PEDOT/PSS) and poly[bis(4-phenyl)(2,4,6-trimethylphenyl)amine] (PTAA). However, PEDOT/PSS suffers from inherent hydrolytic and UV-induced degradation, whereas PTAA exhibits poor surface wettability, posing substantial manufacturing challenges [6–8]. In comparison, nickel oxide (NiO_x), an inorganic wide-bandgap semiconductor, has emerged as a promising alternative hole transport material (HTM) for perovskite photovoltaics owing to its combination of exceptional stability, efficient charge carrier transport, and low-cost processing [9–11]. Yu et al. developed H_2O_2-engineered NiO_x as the HTM, demonstrating that H_2O_2 addition enhances NiO_x films' conductivity and generates abundant surface hydroxyl groups for improved surface wettability. This approach yielded NiO_x-based p-i-n PSCs with a certified PCE of 25.2% [12]. Most recently, Liu et al. reported a molecular hybridization strategy through co-assembling 4,4',4''-nitrilotribenzoic acid (NA) with [4-(3,6-dimethyl-9H-carbazol-9-yl) butyl]phosphonic acid (Me-4PACz) to improve the quality of NiO_x/perovskite interface [13]. They indicated that the molecular hybridization of Me-4PACz with NA significantly promotes charge carrier extraction from the perovskite to NiO_x layer. Consequently, the resulting PSCs achieved a certified steady-state efficiency of 26.54%. This impressive PCE value further validates the potential of NiO_x as an HTM for p-i-n perovskite photovoltaics.

However, it should be noted that most high-efficiency p-i-n PSCs fabricated on NiO_x hole transport layer (HTL) are mainly processed by the one-step deposition method. Although the two-step sequential deposition method is widely regarded as more reproducible and readily scalable, the efficiency of two-step-processed (TSP) p-i-n devices rarely exceeds 24%, demonstrating significantly inferior performance when compared to their one-step counterparts [14, 15]. The fundamental mechanisms underlying the suboptimal performance are primarily attributed to the uncontrollable reaction between pre-deposited PbI_2 and ammonium salts during the two-step sequential deposition process, generating crystalline phase heterogeneity, such as residual PbI_2 clusters at the bottom, within the bulk, and on the surface of the perovskite, which deteriorate device efficiency and stability [16, 17]. To address these challenges, researchers have developed various strategies including additive engineering [18], crystallization modulation [19], and particularly focusing on buried interface engineering [20, 21] to reduce residual PbI_2 cluster formation while simultaneously improving the crystallinity of perovskite films. For example, Zhang et al. introduced a thin layer of CsBr at the top surface of NiO_x before PbI_2 deposition [22]. They suggest that the buried modification of CsBr not only passivated NiO_x surface defects to reduce recombination but also regulated the crystal growth orientation of the upper PbI_2, promoting the subsequent permeation of ammonium salts into the PbI_2 framework to form stable perovskite. With this method, they achieved more uniform and smoother perovskite film with large grain size. Gao et al. developed a pre-embedding mixed A-cation halide strategy to transform the residual PbI_2 near the buried interface into stable 3D perovskite [23]. Moreover, they indicated that this strategy effectively balances lattice strain in the perovskite layer adjacent to the buried interface, contributing to high-efficiency PSCs with superior stability. Nevertheless, Qu et al. demonstrated that residual PbI_2 clusters are predominantly distributed at the top surface of the TSP perovskite film, forming a phase heterogeneity that disrupting vertical charge transport equilibrium [24]. They further established that achieving phase homogeneity in the TSP perovskite film is essential for high device performance. However, the

https://doi.org/10.1007/s40820-025-02010-w

study did not fully clarify the detrimental effects of PbI_2 induced phase heterogeneity, particularly in terms of how PbI_2 cluster-mediated interfacial energy-level mismatches impact the charge transport at the NiO_x/perovskite interface. Besides, a comprehensive understanding of the unique poor performance of NiO_x-based TSP p-i-n PSCs remains crucial yet has rarely been documented.

Herein, we elucidate that residual PbI_2 clusters exhibit vertically gradient distribution across TSP perovskites and mainly accumulate at the top surface of the film. This spatial distribution establishes a Schottky-type heterojunction with $FAPbI_3$ perovskite, which induces upward band bending within the perovskite, resulting in substantial energy-level mismatches at both NiO_x/perovskite and perovskite/C60 interfaces, thus ultimately degrading device performance. To mitigate this problem, we developed a vertical interfacial engineering strategy enabled by the synergistic dual-interface modification of tin trifluoromethanesulfonate ($Sn(OTF)_2$) and 4-fluorophenylethylamine chloride (F-PEA), successfully fabricating high-performance NiO_x-based TSP p-i-n PSCs. Specifically, $Sn(OTF)_2$ was employed as a multifunctional buried interface regulator. The functional –OTF groups demonstrate strong coordination bonds with both NiO_x and residual PbI_2, which not only increases the $Ni^{\geq 3+}/Ni^{2+}$ ratio to enhance NiO_x conductivity but also converts dense PbI_2 into a macroporous structure that facilitates ammonium salt penetration, enabling the fabrication of large grain, highly crystalline perovskite films. Moreover, divalent Sn^{2+} ions readily incorporate into the perovskite lattice, generating a Pb–Sn mixed perovskite interlayer at the NiO_x/perovskite interface. This interlayer effectively elevates the valence band maximum (VBM) of the underlying perovskite from −5.84 to −5.53 eV, achieving precise optimization of the NiO_x/perovskite interfacial energy-level alignment. Complementing the buried interface regulation by $Sn(OTF)_2$, F-PEA targets the top surface residual PbI_2 clusters. It reacts with surface PbI_2 to form a 2D perovskite layer, which not only passivates bulk and surface defects but also modulates the energy-level alignment at the perovskite/C60 interface, directly resolving the interfacial mismatch caused by surface PbI_2. Consequently, owing to the synergistic effects of $Sn(OTF)_2$ and F-PEA modification, the resulting NiO_x-based TSP p-i-n PSCs delivered a champion power conversion efficiency (PCE) up to 25.6%, and the unencapsulated devices exhibited exceptional operational stability with a T_{80} time exceeding 1000 h in a N_2 atmosphere.

2 Experimental and Calculation

2.1 Materials

The ITO substrates, nickel oxide (NiO_x), C60 (99.9%), formamidinium iodide (FAI), and methylammonium iodide (MAI), were purchased from Advanced Election Technology Co., Ltd. The tin trifluoromethanesulfonate ($Sn(OTF)_2$) and BCP were purchased from Alfa Aesar. 4-Fluorophenylethylamine chloride (F-PEA), methylammonium chloride (MACl), and lead iodide (PbI_2) were purchased from Xi'an Yuri Solar Co., Ltd. Dimethyl sulfoxide (DMSO, 99.9%), dimethylformamide (DMF, 99.8%), and isopropanol (IPA, anhydrous, 99.8%) were purchased from Sigma-Aldrich.

2.2 Device Fabrication

ITO glass substrates (7 Ω sq^{-1}) were thoroughly cleaned and treated with plasma for 5 min before usage. A layer of NiO_x (10 mg mL^{-1} in DI water, filtered through a 0.22-μm PTFE syringe filter) was spin coated at 4000 rpm for 30 s without aging, then annealed at 120 °C for 10 min under ambient conditions. After cooling to room temperature, the substrates were transferred to a nitrogen-filled glovebox. The $Sn(OTF)_2$ interlayer was spin coated from the stock solutions (1 mg mL^{-1} in Ethanol) at 3000 rpm for 30 s and annealed at 100 °C for 10 min. Subsequently, a PbI_2 (1.5 M, DMF/DMSO = 9:1) layer was formed on the substrates using spin coating at 2000 rpm for 30 s, annealing at 70 °C for 60 s. After the PbI_2 film was cooled to room temperature, FAI/MAI/MACl (90 mg:6.39 mg:9 mg in 1 mL IPA) was spin coated at 2000 rpm for 30 s, followed by thermal annealing at 150 °C for 15 min in an ambient air self-made glovebox with a relative humidity of 10%. For the F-PEA post-treatment, 2 mg mL^{-1} F-PEA in IPA/DMSO = 95:5 solution was spin coated onto the perovskite surface, followed by thermal annealing at 100 °C for 5 min in a nitrogen-filled glovebox. Finally, the samples were transferred to an evaporation chamber where 30 nm C60 at 0.2 Å s^{-1}, 8 nm BCP at 0.2 Å s^{-1}, and 100 nm Ag at 1.0 Å s^{-1} were deposited under vacuum. The active area of the devices was 0.04 cm^2.

2.3 Characterizations

All samples were well kept in vacuum-sealed bags during sample transfer. The grazing incidence X-ray diffraction

(GIXRD) measurements were conducted on a multifunctional X-ray diffractometer (XPert Pro MPD). Depth-dependent phase information including surface, bulk, and buried interface phases within the perovskite layer can be acquired by adjusting the incident angle (θ) between the X-ray beam and the sample surface. The depth-profiling ultraviolet photoelectron spectroscopy (UPS, ESCALAB 250Xi, Thermo Fisher) measurements were carried out using a He I discharge lamp (21.22 eV). The different etching depths were achieved by a laser marking system. X-ray photoelectron spectroscopy (XPS) was conducted on a Thermo Scientific™ K-Alpha™$^+$ spectrometer equipped with a monochromatic Al Kα X-ray source (1486.6 eV) operating at 100 W. All peaks were calibrated with C 1 *s* peak binding energy at 284.8 eV for adventitious carbon. For the depth-profiling XPS analysis, the spectra were collected after different Ar-sputtering etching time. The XRD patterns (2θ scans) were obtained on Bruker Advanced D8 X-ray diffractometer using Cu Kα (λ = 0.154 nm) radiation. The ^{19}F nuclear magnetic resonance (NMR) spectra were recorded in deuterated dimethyl sulfoxide (DMSO-d6) using a 300 MHz Bruker spectrometer. A UV–Vis spectrophotometer (Agilent Cary 5000) was used to collect the transmittance spectra of the substrates and absorbance spectra of the perovskites. Steady-state photoluminescence (PL) spectra were recorded on Shimadzu RF-5301pc. Time-resolved photoluminescence spectra were measured on a PL system (Fluo-Time 300) under excitation with a picosecond pulsed diode laser at 640 nm wavelength with a repetition frequency of 1 MHz films. The morphology of the films was studied by field-emission scanning electron microscopy (FESEM, TESCAN, MIRA3) and atomic force microscopy (AFM, Bruker Dimension Icon). Current density–voltage (J-V) curves of the devices were collected using a source meter (Keysight B2901A) and a solar simulator (Enlitech SS-F5-3A) with a protocol of 1.2 to −0.1 V with a 20 mV voltage step and 10 ms delay. The light intensity was calibrated to AM 1.5G (100 mW cm^{-2}) by using a reference Si solar cell. The external quantum efficiency (EQE) spectra were recorded with a quantum efficiency measurement system (Enlitech QER-3011) in which the light intensity at every wavelength was calibrated with a Si detector before measurement. The maximum power point (MPP) output was measured by testing the steady-state current density at the maximum power point voltage. Electron only devices with a configuration of ITO/SnO_2/Perovskite/PCBM/Ag were fabricated for SCLC measurement. The J-V responses of the electron-only devices were measured at RT in the dark. Mott–Schottky analyses were conducted using an electrochemical workstation (IM6eX, Zahner, Germany) under dark conditions. Measurements spanned a voltage range of 0 to 1.5 V, with capacitance–voltage (C–V) curves acquired at a fixed frequency of 5 kHz and a small AC perturbation amplitude of 10 mV. The elemental distribution in perovskite film was characterized using PHI nanoTOF II Time-of-Flight SIMs.

2.4 Density Functional Theory Calculations

First-principles calculations were carried out using the Vienna Ab-initio Simulation Package (VASP), employing the projector augmented wave (PAW) method. The Perdew–Burke–Ernzerhof (PBE) functional within the generalized gradient approximation (GGA) was adopted to describe electron exchange and correlation effects. For the calculations of adsorption energy and defect passivation, a plane-wave cutoff energy of 400 eV was employed, with energy and force convergence criteria set to 1×10^{-4} eV and 0.05 eV Å^{-1}, respectively.

The NiO_X (100) surface was modeled using a $3 \times 3 \times 1$ supercell incorporating a vacuum layer of 15 Å, while the $FAPbI_3$ (100) surface was constructed with a $3 \times 3 \times 2$ supercell. A Γ-centered $3 \times 3 \times 1$ Monkhorst–Pack k-point mesh was adopted for the doped NiO_x systems, and $1 \times 1 \times 1$ for the doped $FAPbI_3$ system. The van der Waals interactions were accounted for using the Grimme DFT-D3 with the zero-damping function in adsorption energy calculations. Additionally, the electrostatic potential (ESP) of the -OTF group was computed using all-electron double-ζ valence basis sets. All crystal structures were constructed using Materials Studio and visualized with VESTA.

3 Results and Discussion

3.1 Effects of Vertical Interfacial Engineering on Device Performance

SnO_2-based two-step-processed (TSP) regular n-i-p PSCs have demonstrated high efficiency and reproducibility [25–27]. However, while demonstrating potential for tandem

https://doi.org/10.1007/s40820-025-02010-w

applications, NiO_x-based TSP p-i-n PSCs show significantly inferior photovoltaic performance (Fig. S1) and have been rarely documented. To delve into the underlying mechanisms governing this performance disparity, the phase homogeneity in TSP $FAPbI_3$ perovskite film was investigated using grazing incidence X-ray diffraction (GIXRD) with varying incident angles from 0.5° to 5°. As shown in Fig. 1a, the TSP film exhibits distinct diffraction peaks at 12.8°, which correspond to PbI_2, indicating the existence of residual PbI_2 within the film. Additionally, the diffraction intensity of the PbI_2-related peaks gradually decreases with increasing incident angles. This observation suggests that the residual PbI_2 is predominantly distributed near the top surface of the film. To quantitatively evaluate the distribution of PbI_2, the perovskite film was exfoliated from the substrate (Fig. S2), and X-ray photoelectron spectroscopy (XPS) was conducted to analyze the chemical states at the top and bottom surfaces. As shown in Fig. S3, the bottom surface of the TSP perovskite film exhibits significantly stronger methylammonium (MA^+) and formamidinium (FA^+) cation signals compared to the top surface, corroborating the conclusion that residual PbI_2 is predominantly distributed near the top surface. This is further supported by the Pb 4*f* core-level spectra, which exhibit a lower binding energy shift at the bottom surface, consistent with reduced PbI_2 content as previously reported [24]. Furthermore, depth-profiling XPS was performed to determine the I/Pb ratio across different etching times (Fig. S4 and Table S1). This ratio primarily reflects contributions from $FAPbI_3$ perovskite and residual PbI_2 clusters. As shown in Fig. 1b, increasing etching time raised the I/Pb ratio from 2.56 (0 s) to 2.83 (150 s), which lowered the $PbI_2/FAPbI_3$ ratio from 0.79 to 0.2. These results indicate a higher proportion of $FAPbI_3$ and less PbI_2 with increasing etching time, further confirming that residual PbI_2 is mainly distributed near the top surface of the TSP film, consistent with previous studies. As illustrated in Fig. 1c, the residual PbI_2, as a wide-bandgap semiconductor, tends to form a Schottky contact with $FAPbI_3$, resulting in a band bending in the perovskite [28]. Consequently, the inhomogeneous PbI_2 distribution disrupts the vertical energy-level alignment in perovskites, thereby impairing charge carrier transport and device efficiency [29].

To this end, a vertical interfacial engineering enabled by dual-interface modification was developed to fabricate high-performance NiO_x-based TSP p-i-n PSCs. As depicted in Fig. 1d, functional tin trifluoromethanesulfonate ($Sn(OTF)_2$) and 4-Fluorophenylethylamine chloride (F-PEA) were spin coated onto NiO_x and perovskite surface, respectively, as interfacial layers during device fabrication. Their working mechanisms are schematically illustrated in Fig. 1e-g. Depositing pristine TSP films on bare NiO_x (denoted as the control) introduces abundant defects at the NiO_x/perovskite interface, including oxygen vacancies (V_O), undercoordinated $Ni^{\geq 3+}$ species, iodine vacancies (V_I), and Pb vacancies (V_{Pb}). These defects facilitate adverse redox reactions, accelerate ion migration from the perovskite layer to NiO_x, and ultimately degrade device performance (Fig. 1e) [30]. Besides, the compact pre-deposited PbI_2 film hinders ammonium salt penetration, leaving control films with numerous heterogeneously distributed residual PbI_2 clusters [31]. Intriguingly, with the introduction of the $Sn(OTF)_2$ interlayer (referred to as $Sn(OTF)_2$ hereafter), the aforementioned adverse redox reactions and ions migration are effectively suppressed via the passivation effect originated from the –OTF groups. Moreover, the divalent Sn^{2+} ions in $Sn(OTF)_2$ can partially compensate for V_{Pb} through incorporation into the perovskite lattice (Fig. 1f), forming a Pb–Sn mixed perovskite interlayer which is critical for energy-level alignment at the buried NiO_x/perovskite interface. Simultaneously, the trifluoromethanesulfonate –OTF groups exhibit strong coordination with PbI_2 through $-SO_3^-\ldots$Pb ionic bonding and $-CF_3\ldots$Pb hydrogen bonding, as evidenced by the ^{19}F NMR spectra (Fig. S5) [32]. This interaction slows PbI_2 crystallization and yields a uniform macroporous PbI_2 framework as evidenced by the XRD amd SEM results (Fig. S6). This enhances ammonium salt penetration and reduces residual PbI_2 clusters at the interface. Finally, F-PEA post-treatment induces the formation of 2D perovskite capping layer at the top surface of the perovskite (referred to as $Sn(OTF)_2$ + PEA hereafter, Fig. 1g) [33]. The formation of this 2D perovskite not only reduces residual PbI_2 clusters near the top surface of the film but also passivates defects and optimizes energy-level alignment at the perovskite/C60 interface. Building on these advantages, it is expected that the vertical interfacial engineering can significantly enhance the efficiency and stability of the resulting NiO_x-based TSP p-i-n PSCs.

To evaluate the efficacy of the $Sn(OTF)_2$ interlayer and F-PEA post-treatment on device performance, NiO_x-based TSP p-i-n PSCs (Fig. 1d) were fabricated. The corresponding cross-sectional SEM image of the device exhibits a uniform stacking of functional layers (Fig. S7). Figure 1h

summarizes statistical photovoltaic parameters of the devices based on the control, $Sn(OTF)_2$, and $Sn(OTF)_2$ + PEA films. It is found that the $Sn(OTF)_2$ + PEA devices demonstrate an overall enhancement on open-circuit voltage (V_{oc}), short-circuit current density (J_{sc}), and fill factor (FF), resulting in the best PCEs. Figures 1i and S8a–c show the photocurrent density–voltage (J-V) curves of the champion devices, corresponding photovoltaic parameters are summarized in Table S2. Hysteresis analysis based on H-index (HI) reveals that the $Sn(OTF)_2$ + PEA device has the smallest HI value (1.9%) compared to the control (9.3%) and $Sn(OTF)_2$ (4.7%) devices. The external quantum efficiency (EQE) integrated J_{sc} is 23.51, 24.34, and 25.16 mA cm^{-2} for the control, $Sn(OTF)_2$, and $Sn(OTF)_2$ + PEA devices, respectively, which is well matched with the J_{sc} extracted from the J-V curves (Fig. S8d). To confirm the reliability of the J-V measurements, steady-state power output (SPO) at the maximum power point was recorded (Fig. S8e). The PCE of the control, $Sn(OTF)_2$, and $Sn(OTF)_2$ + PEA devices stabilized at 20.1%, 23.2%, and 25.1%, respectively, which are consistent with the J-V results. Besides, it should be mentioned that the $Sn(OTF)_2$ + PEA device gave a champion PCE of 25.6% under reverse scan with a V_{oc} of 1.18 V, a J_{sc} of 26.1 mA cm^{-2}, an FF of 82.8%. This PCE represents one of the highest efficiencies recorded for TSP p-i-n structured PSCs thus far (Fig. 1j).

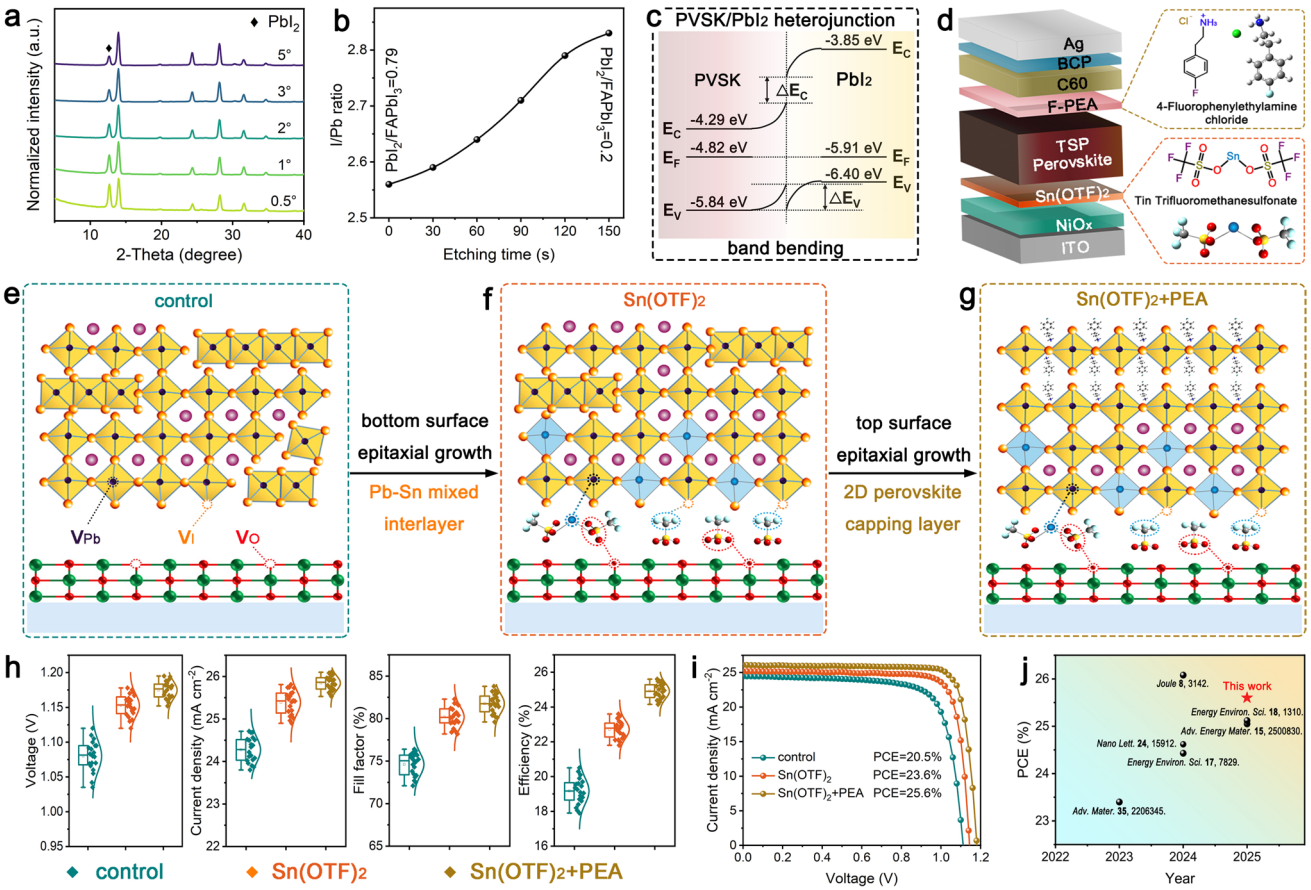

Fig. 1 **a** GIXRD patterns of the TSP films with varying incident angles. **b** I/Pb ratio of the TSP film with varying etching time. **c** Schottky junction between PbI_2 and perovskite. **d** Schematic structure of the NiO_x-based TSP p-i-n PSCs, and chemical structure of the $Sn(OTF)_2$ and F-PEA. Crystallization process of **e** control, **f** $Sn(OTF)_2$, and **g** $Sn(OTF)_2$ + PEA perovskites. **h** Statistical photovoltaic parameters for different PSCs. A total of 20 devices in 3 batches for each sample were counted. **i** J-V curves of the champion devices based on the control, $Sn(OTF)_2$, and $Sn(OTF)_2$ + PEA films. **j** Efficiency progress of TSP p-i-n structured PSCs over recent years

https://doi.org/10.1007/s40820-025-02010-w

3.2 Influence of $Sn(OTF)_2$ on the Properties of NiO_x

To elucidate the dual-anchoring capability of $Sn(OTF)_2$ at the NiO_x/perovskite interface and its passivation effects on the perovskite layer, density functional theory (DFT) calculations were conducted using the Vienna Ab-initio Simulation Package (VASP). The calculations specifically focus on the functional –OTF groups. As shown in the inset of Fig. 2a, the electrostatic potential surface (EPS) of the –OTF group reveals a strong electron-withdrawing region (red, negative potential) localized around the $–SO_3^-$ group, while the electron-donating region (blue, positive potential) is primarily localized near the $–CF_3$ end. The oxygen atoms in the $–SO_3^-$ group can effectively coordinate with undercoordinated Ni^{3+} or Pb^{2+} ions at the NiO_x/perovskite interface, thereby reducing defect-induced trap states. To evaluate the anchoring preference of the –OTF group, adsorption energies (E_{ad}) were calculated for both terminal groups ($–SO_3^-$ and $–CF_3$) on NiO_x (001) and perovskite (001) surfaces (Fig. S9). The $–SO_3^-$ group demonstrates a substantially lower E_{ad} value on NiO_x (− 5.02 eV) compared to the $–CF_3$ group (− 2.36 eV), indicating a significantly stronger binding affinity toward the NiO_x surface. Conversely, both moieties displayed weaker binding on the perovskite (001) surface, with E_{ad} values of − 1.98 eV for $–SO_3^-$ and − 1.01 eV for $–CF_3$. These computational results demonstrate that –OTF groups exhibit two distinct adsorption modes at the NiO_x surface. The majority of $–SO_3^-$ moieties preferentially anchor to the NiO_x surface, while $–CF_3$ interact specifically with undercoordinated Pb^{2+} sites in adjacent perovskite layers, establishing dual-anchoring behavior. However, in regions with either incomplete NiO_x coverage or excessive—OTF loading (over-coverage), residual unbound—SO_3^- groups may interact with the perovskite surfaces through ionic bonding, enhancing interfacial connectivity while optimizing structural configuration.

It has been reported that under continuous illumination or applied electric fields, iodine vacancies (V_I) readily form on perovskite surfaces [34]. These vacancies trap excess electrons and facilitate Pb-Pb dimer formation via attractive interactions between adjacent Pb atoms, thereby compromising structural stability [35]. As shown in Fig. 2b, these dimers introduce deep-level trap states within the bandgap, enhancing non-radiative recombination and decreasing carrier lifetimes [36]. The –OTF groups mitigate this issue through interaction with Pb^{2+}, effectively passivating trap states and restoring a clean bandgap. DFT results demonstrate a substantial increase in Pb–Pb interatomic distance from 3.65 to 6.49 Å following –OTF passivation (Fig. 2c), providing direct evidence of dimer dissociation. Additionally, owing to the strong affinity of the $–SO_3^-$ group for NiO_x, the differential charge density (Δρ) at the –OTF/NiO_x interface was analyzed. Figure 2d demonstrates that $–SO_3^-$ group interacts with NiO_x through S = O···Ni coordination bonds, resulting in electron depletion on NiO_x and accumulation on –OTF. This charge redistribution facilitates hole transfer to NiO_x, thereby improving interfacial charge extraction efficiency.

Fourier-transform infrared (FTIR) spectroscopy was adopted to experimentally study the above-mentioned interactions. As presented in Fig. 2e, the S = O and S–O stretching vibrations of pure $Sn(OTF)_2$ exhibited red shifts from 1226 to 1222 cm^{-1} and 1019 to 1014 cm^{-1}, respectively, in the $NiO_x + Sn(OTF)_2$ sample. This lower wavenumber shifted S = O and S–O peaks validate the interaction between NiO_x and the $–SO_3^-$ group. Besides, XPS measurement was conducted to analyze the chemical states of the deposited NiO_x and $NiO_x/Sn(OTF)_2$ thin films. The detection of a distinct S 2*p* XPS peak (Fig. 2f) confirms the successful introduction of $Sn(OTF)_2$ onto the NiO_x surface. Figure 2g shows the Ni $2p_{3/2}$ core spectra of the films, which were deconvoluted into three peaks corresponding to satellite states, $Ni^{\geq 3+}$ and Ni^{2+} species [37]. Notably, the Ni $2p_{3/2}$ core spectra of the $NiO_x/Sn(OTF)_2$ film exhibit a positive binding energy shift, corroborating the interaction between NiO_x and $Sn(OTF)_2$. Furthermore, as determined by the integral areas of the respective peaks, the $Ni^{\geq 3+}/Ni^{2+}$ ratio increased from 1.87 to 2.03 for the NiO_x and $NiO_x/Sn(OTF)_2$ films, respectively, which can be attributed to electron transfer from Ni to electron-withdrawing $–SO_3^-$ groups. In general, higher $Ni^{\geq 3+}$ content in NiO_x films correlates with improved electrical conductivity [12]. To quantify this, current–voltage (I-V) measurements were conducted on devices with the architecture illustrated in the inset of Fig. 2h, with detailed calculations and parameters summarized in Table S3. Accordingly, the $NiO_x/Sn(OTF)_2$ film demonstrates significantly enhanced conductivity (2.6×10^{-5} S cm^{-1}) compared to bare NiO_x (2.0×10^{-5} S cm^{-1}), which is beneficial for hole transport.

Subsequently, the surface properties of NiO_x and $NiO_x/Sn(OTF)_2$ films were systematically investigated. Figure S10 presents the surface morphology and roughness of the films. The scanning electron microscopy (SEM) images indicate

that $Sn(OTF)_2$ does not alter the morphology of NiO_x films. In contrast, atomic force microscopy (AFM) results demonstrate a reduction in surface roughness, with root-mean-square (RMS) roughness decreasing from 5.29 ± 0.34 nm (bare NiO_x) to 4.76 ± 0.18 nm ($NiO_x/Sn(OTF)_2$). This roughness reduction confirms the formation of a continuous and pinhole-free $Sn(OTF)_2$ interlayer, which is a prerequisite for its passivation and coordination functions. Furthermore, the reduced RMS roughness eliminates localized peaks/valleys, ensuring uniform coverage of the perovskite layer on the NiO_x surface and maximal contact with the $Sn(OTF)_2$ interlayer, which is critical for charge carrier extraction [38]. Further, Kelvin probe microscopy (KPFM) measurements were conducted to evaluate the surface potential of the films. As shown in Fig. 2i, j, contact potential difference (CPD) values for NiO_x and $NiO_x/Sn(OTF)_2$ films were 75 and 12 mV, respectively. The lower CPD value in $NiO_x/Sn(OTF)_2$ film indicates a larger work function compared to the bare NiO_x [39, 40]. To quantitatively assess film work functions, ultraviolet photoelectron spectroscopy (UPS) measurements were performed. Figure 2k presents the secondary electron cutoff (E_{cutoff}) energies of the NiO_x and $NiO_x/Sn(OTF)_2$ films, from which the corresponding Fermi level (E_F) values were determined to be -4.62 and -4.79 eV, respectively. The downward-shifted E_F in $NiO_x/Sn(OTF)_2$ film confirms the increased work function, which is consistent with the KPFM results. Figure 2l shows the energy gap between the VBM and E_F of the films. A smaller gap (0.68 eV) in $NiO_x/Sn(OTF)_2$ film indicates stronger p-type doping, correlating with the higher $Ni^{\geq 3+}/Ni^{2+}$ ratio observed via XPS. Consequently, the $NiO_x/Sn(OTF)_2$ film demonstrated a deeper VBM (-5.47 eV) than that of bare NiO_x film (-5.33 eV,

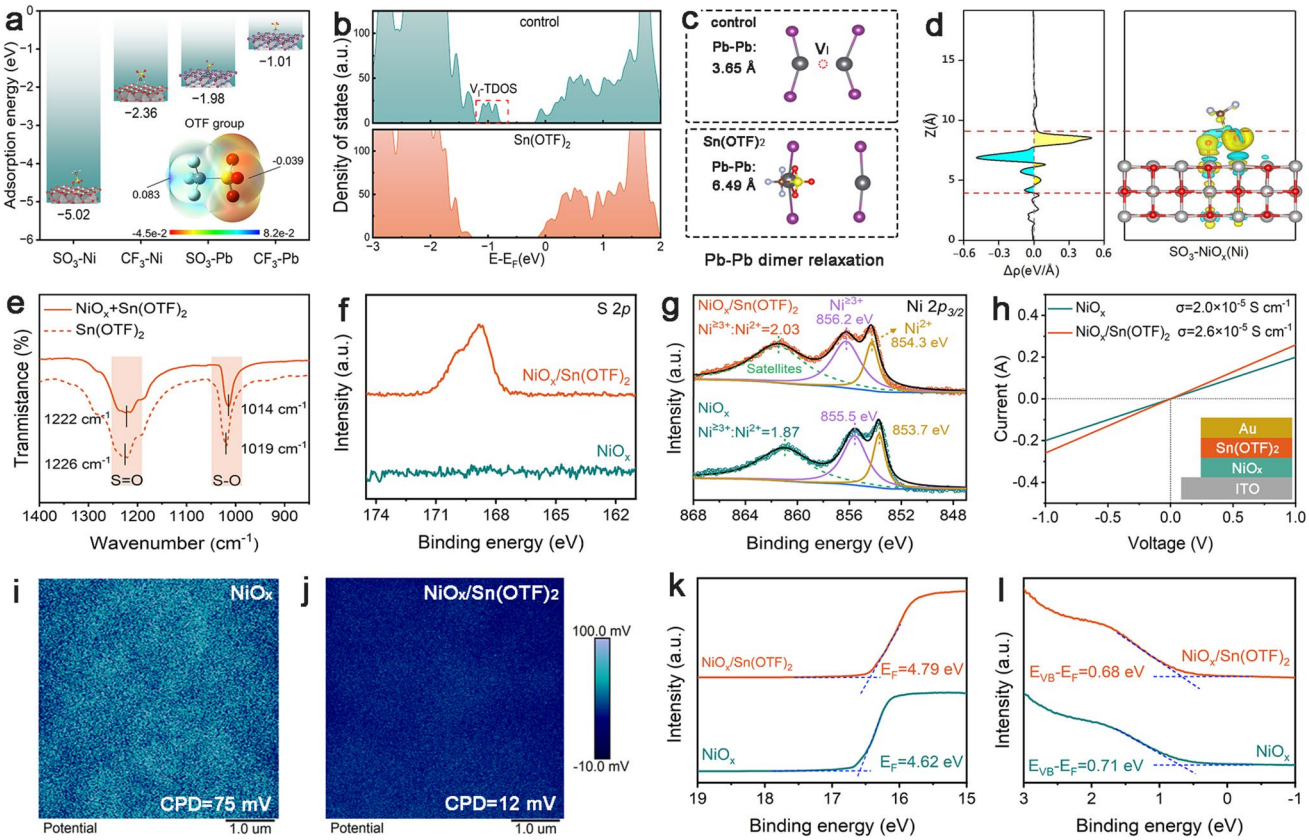

Fig. 2 **a** Adsorption energies of $-SO_3^-$ and $-CF_3$ groups with NiO_x and perovskite, and the electrostatic potential profile of the –OTF group. **b** The density of states of the surface electron-injected V_I defect for the control and $Sn(OTF)_2$ films. **c** Schematic diagram of an iodine vacancy with trapping an electron to form a Pb – Pb dimer and then passivated by $Sn(OTF)_2$. **d** Differential charge density mapping depicting the interaction of the $-SO_3^-$ group with the NiO_x layer. **e** FTIR spectra of pure $Sn(OTF)_2$ and $NiO_x + Sn(OTF)_2$. XPS core spectra of **f** S 2*p* and **g** Ni $2p_{3/2}$ for bare NiO_x and $NiO_x/Sn(OTF)_2$ films. **h** I-V characteristics of the different films for evaluating the corresponding conductivity. KPFM images of **i** bare NiO_x and **j** $NiO_x/Sn(OTF)_2$ films. UPS spectra of secondary electron **k** cutoff (E_{cutoff}) and **l** onset (E_{onset}) energy

https://doi.org/10.1007/s40820-025-02010-w

Table S4). This energy-level adjustment is essential for mitigating the energy-level mismatch at the NiO_x/perovskite interface. Additionally, Fig. S11 presents the optical transmission spectra of films deposited on Glass/indium tin oxide (ITO) substrates. Both NiO_x and NiO_x/$Sn(OTF)_2$ films exhibit high transmittance across the visible spectrum, which is favorable for highly efficient PSCs fabrication.

3.3 Effects of Dual-Interface Modification on Perovskite Crystallization and Properties

Due to the direct contact with $Sn(OTF)_2$ interlayer, the crystallization and quality of the perovskite should be affected [41]. To delve into the effect of the $Sn(OTF)_2$ interlayer on TSP perovskite crystallization, in situ photoluminescence (PL) spectroscopy was conducted. As shown in Fig. S12, the perovskite PL peak ($\lambda = 800$ nm) for the control film emerges within 5 s of annealing, and the PL intensity saturates at approximately 20 s, indicating complete crystallization. This rapid rate corresponds to the abundant nucleation sites in dense PbI_2, resulting in swift perovskite formation. In contrast, for the $Sn(OTF)_2$ film, an initial PL peak at $\lambda = 850$ nm (5–10 s) corresponds to early-stage Pb–Sn perovskite, indicating the incorporation of Sn^{2+} from $Sn(OTF)_2$ into the lattice. Subsequently, the peak shifts to $\lambda = 800$ nm as the organic salts (FAI, MAI, and MACl) fully diffuse and react, signifying mature perovskite formation. The corresponding PL intensity saturates at around 30 s, which is 50% longer than that of the control. This slower rate aligns with the reduced nucleation density of the porous PbI_2 template, leading to longer grain growth times but larger grain sizes. To validate the enlarged perovskite grains, the perovskite films were exfoliated from the substrates. Figure 3a shows bottom-view SEM images of the control and $Sn(OTF)_2$ films. It is noticeable that the control film exhibits a bottom surface morphology with small grains and minor pinholes, whereas the $Sn(OTF)_2$ film features a pinhole-free bottom surface morphology with significantly larger grains, which is in accordance with the in situ PL results. Corresponding AFM images (Fig. 3b) of the perovskites suggest that $Sn(OTF)_2$ film exhibits a smoother bottom surface (RMS = 16.9 nm), demonstrating improved interfacial contact between the perovskite layer and substrate, which is beneficial for high device performance [42]. The increase in perovskite grain size, decrease in pinhole density, and reduction in RMS roughness observed in the $Sn(OTF)_2$ film stems primarily from the –OTF functional groups of $Sn(OTF)_2$. These functional groups coordinate with PbI_2, inducing the formation of a uniform macroporous PbI_2 film (Fig. S6). This facilitates organic salt diffusion throughout the film and promotes perovskite nucleation and growth of larger grains. Bottom surface GIXRD measurements were conducted to investigate the structural properties of the films. As shown in Fig. S13, the $Sn(OTF)_2$ film exhibits a much weaker PbI_2 peak intensity than the control film at the same incident angles. This observation indicates that the $Sn(OTF)_2$ interlayer facilitates the transformation from PbI_2 to perovskite, resulting in highly crystalline perovskite film with reduced residual PbI_2 clusters at the bottom. Additionally, the enlarged (100) perovskite planes (Fig. 3c) reveal peak shifts toward higher angles in the $Sn(OTF)_2$ film at incident angles lower than 3°. This implies Sn^{2+} ions (with smaller ionic radii) have incorporated into the perovskite lattice, forming a Pb–Sn mixed perovskite phase. As the incident angles increased beyond 3°, no significant peak shift can be observed, suggesting that the Pb–Sn mixed perovskite layer is predominantly distributed near the bottom surface of the $Sn(OTF)_2$ perovskite film. To further validate the incorporation of Sn^{2+} ions, high-resolution transmission electron microscopy (HRTEM) analysis was performed (Fig. 3d). It is noteworthy that well-defined lattice fringes of perovskite crystal can be found, indicating excellent crystallinity. Besides, the measured (100) d-spacing of 6.1 Å is relatively smaller than that of pure Pb-based perovskite (6.3 Å), consistent with the substitution of Pb^{2+} (ionic radius 1.19 Å) by smaller Sn^{2+} ions (1.10 Å). Furthermore, high-angle annular dark-field (HAADF) energy-dispersive X-ray spectroscopy (EDXS) elemental mappings of the perovskite crystal (Fig. 3e) demonstrate uniform spatial distributions of I, Br, N, and Pb. Critically, the distinct Sn signal provides direct evidence for successful Sn^{2+} incorporation in the final perovskite film.

Besides, the chemical states at the bottom surface of the perovskites were also investigated. As presented in Fig. 3f, the Pb 4*f* core spectra in the $Sn(OTF)_2$ film exhibit a lower binding energy shift compared to the control film. This binding energy shift is mainly attributed to synergistic interactions between $–SO_3^-$ and $–CF_3$ groups (from –OTF groups) with PbI_2, as evidenced by combined ^{19}F NMR analysis (Fig. S5) and DFT-calculated adsorption energies (Fig. S9). These interactions effectively passivate V_I defects, consistent with the defect passivation mechanism

demonstrated in our DFT simulations (Fig. 2b). Moreover, the detection of distinct Sn 3*d* XPS peaks (Fig. 3g) in the $Sn(OTF)_2$ film further confirms the successful incorporation of Sn^{2+} ions into the perovskite lattice. The Sn/Pb atomic ratio N_{Sn}/N_{Pb} was calculated as 0.11 according to the equation: $N_{Sn}/N_{Pb} = \left(A_{Sn}/S_{Sn}\right)/\left(A_{Pb}/S_{Pb}\right)$, where A_{Sn} (50,142) and A_{Pb} (775,635) represent the Sn 3*d* and Pb 4*f* peak areas, and S_{Sn} (4.095) and S_{Pb} (6.968) are their respective sensitivity factors [43]. This indicates that the bottom Pb–Sn mixed perovskite interlayer owns a composition of $FASn_{0.1}Pb_{0.9}I_3$. According to previous studies [44], the VBM of Pb–Sn perovskite is determined by interactions between Sn-*s* and I-*p* orbitals, leading to VBM positions higher than their Pb-only counterparts. Thus, the $FASn_{0.1}Pb_{0.9}I_3$ perovskite interlayer effectively elevates the VBM of the perovskite, which critically optimizing NiO_x/perovskite interfacial energy-level alignment. Additionally, depth-profiling XPS measurements were performed to determine the thickness of the $FASn_{0.1}Pb_{0.9}I_3$ interlayer. As shown in Fig. 3h, the peak intensity of the Sn 3*d* spectra progressively decreases with increasing etching time and disappears entirely after 50 s of etching. Based on the measured thickness of the perovskite film (700 nm, Fig. S7) and the Pb 4*f* depth profile (Fig. S14), the thickness of the $FASn_{0.1}Pb_{0.9}I_3$ interlayer was calculated to be approximately 106 nm.

To further investigate the effect of $Sn(OTF)_2$ interlayer and F-PEA post-treatment on perovskite crystallinity, XRD measurements were conducted. As presented in Fig. 4a, all films show distinct diffraction peaks corresponding to the perovskite phase. The $Sn(OTF)_2$ + PEA film displays the strongest (100) perovskite peak and weakest PbI_2 peak, indicating superior crystallinity and the lowest residual PbI_2 content. Additionally, a new diffraction peak at around 5.2° in the $Sn(OTF)_2$ + PEA film confirms the formation of 2D perovskite, which originating from reactions between F-PEA and residual PbI_2 clusters at the perovskite top surface [33]. The UV–visible absorption spectra of the perovskite films are presented in Fig. S15. Notably, the $Sn(OTF)_2$ + PEA film exhibits the strongest absorption across the visible region, which can be attributed to its superior crystallinity. Additionally, the Urbach tail defects in the films were evaluated, and the $Sn(OTF)_2$ + PEA film yielded the smallest Urbach energy (E_u) of 36.5 meV. This low E_u value indicates enhanced crystallinity, which is consistent with the XRD results [45]. Figure 4b displays the steady-state photoluminescence (PL) spectra of the films deposited on quartz glass. The characteristic emission peak is observed at 795 nm, which correlates well with the UV–Vis absorption results. The strongest PL intensity indicates that the non-radiative recombination is substantially suppressed within the $Sn(OTF)_2$ + PEA film. Time-resolved PL (TRPL) measurements were performed to evaluate charge carrier lifetimes, and the results were analyzed using a biexponential decay function, with detailed parameters provided in Table S5. As shown in Fig. 4c, the calculated average carrier lifetimes of the control, $Sn(OTF)_2$, and $Sn(OTF)_2$ + PEA films were 327.9, 565.2, and 756.6 ns, respectively. The longest carrier lifetime in the $Sn(OTF)_2$ + PEA film is primarily ascribed to the enhanced crystallinity and suppressed non-radiative recombination [46].

The surface morphologies of the different perovskite films were investigated using top-view SEM and AFM. As presented in Fig. 4d–f, the $Sn(OTF)_2$ + PEA film exhibits significantly larger grain sizes (exceeding 2 μm) compared to the control (below 1 μm) and $Sn(OTF)_2$ films (approximately 1 μm). This distinct difference in morphology primarily arises from the recrystallization process mediated by F-PEA post-treatment, resulting in the formation of 2D perovskite capping layer, as supported by the XRD results. Figure S16 shows the RMS values of the control, $Sn(OTF)_2$, and $Sn(OTF)_2$ + PEA films, which are 39.9, 37.2, and 33.7 nm, respectively. The $Sn(OTF)_2$ + PEA film exhibits the smallest surface roughness, which is crucial for achieving high device performance. Corresponding KPFM results (Fig. 4g–i) reveal a reduction in CPD values from 281 mV for the control film to 232 mV for the $Sn(OTF)_2$ film and 210 mV for the $Sn(OTF)_2$ + PEA film. As discussed earlier, a decrease in CPD values correlates with an increase in the work function of the respective films, which facilitates balanced energy-level alignment at the perovskite/C_{60} interface. Additionally, the line profiles of the control and $Sn(OTF)_2$ films exhibit significant variations than those of the $Sn(OTF)_2$ + PEA film. These variations can be attributed to a high density of defects on the surface of these perovskite film. Thus, the mitigated CPD variation in the $Sn(OTF)_2$ + PEA film indicates that F-PEA post-treatment effectively passivates surface defects.

https://doi.org/10.1007/s40820-025-02010-w

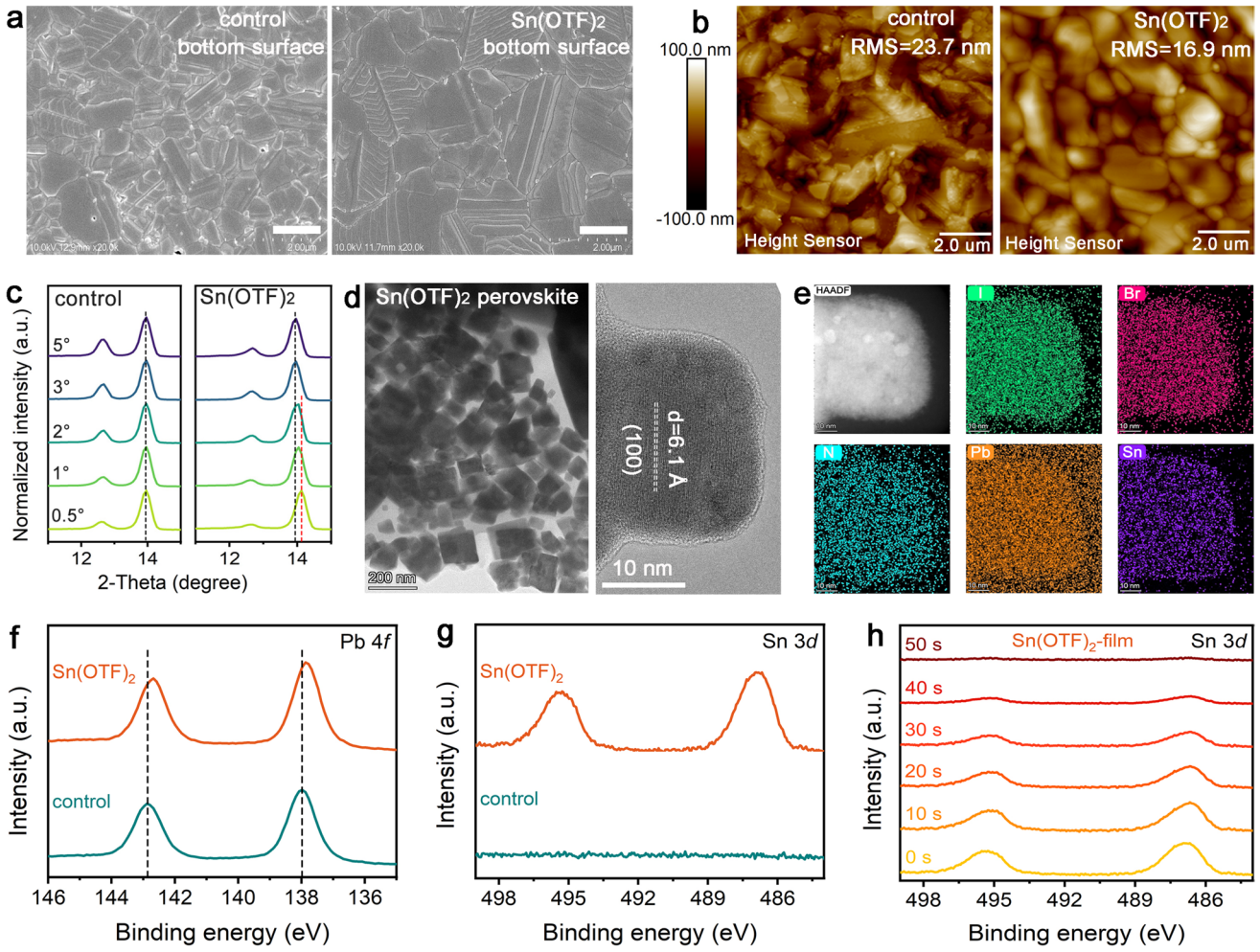

Fig. 3 Bottom-view **a** SEM images and **b** AFM images of the control and $Sn(OTF)_2$ films. **c** Enlarged GIXRD spectra of the control and $Sn(OTF)_2$ films acquired from the bottom surface. **d** TEM image and **e** EDXS mapping of key elements in HAADF mode for $Sn(OTF)_2$ perovskite crystal. **f** Pb 4*f* and **g** Sn 3*d* core spectra of the control and $Sn(OTF)_2$ films. **h** Depth-profiled Sn 3*d* core spectra of the $Sn(OTF)_2$ film with varying etching time

3.4 Energy-Level Alignment and Charge Dynamic Studies

To comprehensively investigate the effects of the $Sn(OTF)_2$ interlayer and F-PEA post-treatment on the energy-level structure of perovskite, depth-profiling UPS measurements were performed to determine the energy-level positions of the control, $Sn(OTF)_2$, and $Sn(OTF)_2$ + PEA perovskite films at varying etching depths. Figure 5a–c presents the obtained E_{cutoff} and E_{onset} spectra for the different films. By combining with the optical bandgap of pure $FAPbI_3$ and the bottom $FASn_{0.1}Pb_{0.9}I_3$ perovskite (Fig. S17), the spatial evolution of the CBM, VBM, and E_F across the depth profile of the films was determined. The corresponding energy-level alignment plots and electronic parameters are presented in Fig. S18 and summarized in Tables S6-S8. Accordingly, the energy-level mismatches at NiO_x/perovskite and perovskite/C60 interfaces were constructed and depicted in Fig. 5d, e, respectively. Notably, the control perovskite exhibits significant energy-level mismatch at the NiO_x/perovskite (0.31 eV) interface (Fig. 5d). In contrast, the incorporation of the $Sn(OTF)_2$ interlayer simultaneously lowers the VBM of NiO_x from −5.33 to −5.47 eV and elevates the VBM of the bottom perovskite from −5.84 to −5.54 eV for $Sn(OTF)_2$ and −5.53 eV for $Sn(OTF)_2$ + PEA. The underlying mechanisms were previously discussed in Figs. 2l and 3g. This

modification reduces the energy-level difference at the NiO_x/perovskite interface to < 0.10 eV, significantly smaller than the 0.31 eV observed in the control device. Furthermore, the F-PEA post-treatment induces formation of 2D perovskite capping layer, enabling the $Sn(OTF)_2$ + PEA film to exhibit a substantially reduced energy-level difference of 0.48 eV at the perovskite/C60 interface (Fig. 5e). This value is markedly lower than those of the control (0.70 eV) and $Sn(OTF)_2$ (0.67 eV) films. Therefore, with the synergistic contributions of the $Sn(OTF)_2$ interlayer and F-PEA post-treatment, the TSP p-i-n PSCs based on the $Sn(OTF)_2$ + PEA film achieve optimized energy-level alignment at both NiO_x/perovskite and perovskite/C60 interfaces. This dual-interface optimization establishes a favorable charge extraction environment while suppressing non-radiative recombination, ultimately yielding the highest device efficiency of 25.6%.

To further understand the notable enhancement in device efficiency, the charge dynamics of the fabricated devices were systematically analyzed. The dependence of V_{oc} and J_{sc} on light intensity (I) was investigated to evaluate the charge carrier recombination and extraction efficiency. As presented in Fig. 5f, the $Sn(OTF)_2$ + PEA device demonstrates the smallest V_{oc} versus I slope (1.31 kT q^{-1}) compared to the control (2.05 kT q^{-1}) and $Sn(OTF)_2$ (1.53 kT q^{-1}) devices, suggesting effective suppression of trap-assisted recombination within the $Sn(OTF)_2$ + PEA device, which typically results in an enhancement of V_{oc} [47]. The analytical results of J_{sc} dependence on I (Fig. S19) indicate that

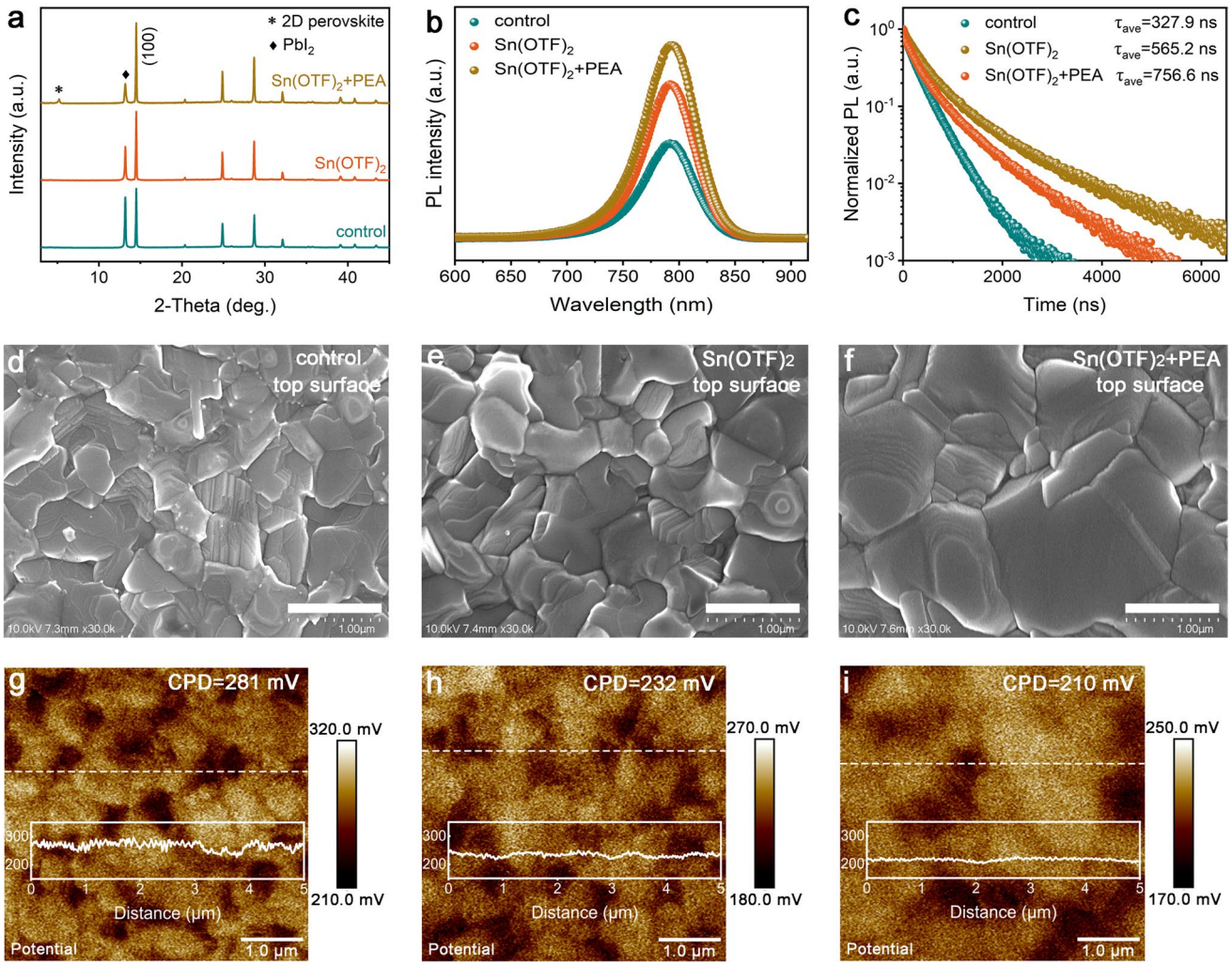

Fig. 4 **a** XRD patterns, **b** steady-state PL spectra, and **c** TRPL spectra of the control, $Sn(OTF)_2$, and $Sn(OTF)_2$ + PEA films. **d-f** Top-view SEM images and **g-i** KPFM images of the different films. The scale bar is 1 μm

https://doi.org/10.1007/s40820-025-02010-w

the $Sn(OTF)_2$ + PEA device delivers the most ideal α value (0.957), demonstrating improved charge carrier extraction efficiency [48]. In addition, the defect density of the perovskite films was quantitatively estimated using space-charge-limited current (SCLC) technique [49]. Figure 5g displays the dark J-V curves of typical electron-only devices (ITO/SnO_2/perovskite/[6, 6]-phenyl-C61-butyric acid methyl ester (PCBM)/Ag) fabricated with different films. Notably, the $Sn(OTF)_2$ + PEA device yields a trap-filled limit voltage (V_{TFL}) of 0.39 V, lower than those of the control (0.64 V) and $Sn(OTF)_2$ (0.47 V) devices. As detailedly described and summarized in Table S9, the defect density was determined. The $Sn(OTF)_2$ + PEA device exhibits the lowest trap state density (4.21×10^{15} cm^{-3}), representing a 39.1% reduction compared to the control (6.91×10^{15} cm^{-3}). While $Sn(OTF)_2$ alone passivates buried interface defects, achieving a reduced defect density of 5.07×10^{15} cm^{-3} (corresponding to a 26.6% reduction in N_t), the additional 12.5% reduction from F-PEA treatment confirms effect surface defect passivation. This surface defect passivation originates from fluorine's high electronegativity, which withdraws electron density from the phenyl ring and enhances the positive charge on the ammonium group ($–NH_3^+$) of the $F\text{-}PEA^+$ cation. The enhanced charge density strengthens the ionic bonding with negatively charged undercoordinated iodide ions (I^-) on the perovskite surface. Concurrently, the lone electron pairs on the fluorine atom form stronger coordinate bonds with undercoordinated Pb^{2+} defects [50]. This dual interaction enables more effective defect passivation. Besides, Mott–Schottky analysis of capacitance–voltage (C-V) characteristics was utilized to investigate the influence of the $Sn(OTF)_2$ interlayer and F-PEA post-treatment on the built-in potential (V_{bi}) of the devices. According to the following equation [51]:

$$\frac{1}{C^2} = \frac{2(V_{bi} - V)}{A^2 q \varepsilon \varepsilon_0 N} \quad (1)$$

where C is the depletion-layer capacitance, ε is the relative permittivity, ε_0 is the vacuum permittivity, A is the active area of the device, N denotes the density of excited states, and V is the applied voltage, the V_{bi} of the devices increases sequentially from 0.91 V (control) to 1.01 V ($Sn(OTF)_2$) and further to 1.04 V ($Sn(OTF)_2$ + PEA), as shown in Fig. 5h. This enhancement in V_{bi} is primarily attributed to the optimized energy-level alignment, which promotes efficient charge carrier separation and extraction, thereby contributing to improved V_{oc} in PSCs. Overall, the notable improvement in photovoltaic performance observed for the $Sn(OTF)_2$ + PEA devices stem from several key factors, including effective suppression of charge recombination, improved charge extraction efficiency, reduced defect density, and optimized interfacial energy-level alignment.

3.5 Effects of Dual-Interface Modification on Device Stability

Furthermore, comprehensive stability assessments of unencapsulated devices under various environmental conditions were performed to evaluate the effects of the $Sn(OTF)_2$ interlayer and F-PEA post-treatment on device stability. As shown in Fig. 6a, the control device rapidly degraded to 80% of its initial PCE (T_{80} = 456 h) under ambient conditions (30%-40% RH). In contrast, the $Sn(OTF)_2$ device exhibited significantly improved stability (T_{80} = 816 h), attributable to its superior perovskite film morphology featuring enlarged crystalline grains and reduced grain boundaries (Fig. 3a), which effectively limit moisture penetration. Notably, after F-PEA post-treatment, the resulting $Sn(OTF)_2$ + PEA device achieves an extended T_{80} lifetime exceeding 1080 h under the same conditions. This significant improvement in ambient stability stems primarily from increased hydrophobicity, as evidenced by contact angle measurements (Fig. S20). It should be noted that Sn^{2+} in tin-based perovskites is highly susceptible to oxidation to Sn^{4+}, as reported, which induces severe non-radiative recombination and structural degradation, ultimately compromising device efficiency and stability [52]. However, in this work, the oxidation of Sn^{2+} in the Pb–Sn mixed perovskite interlayer was effectively suppressed via three strategies: First, $Sn(OTF)_2$ was deposited in an N_2-filled glovebox to prevent oxidation induced by ambient oxygen. Second, undercoordinated $Ni^{\geq 3+}$ species on the NiO_x surface were effectively passivated by –OTF groups, as discussed earlier. Third, the highly crystalline perovskite film reduces defect-induced reactive oxygen species (ROS) generation, which can oxidize Sn^{2+}. To validate the suppressed Sn^{2+} oxidation, unencapsulated perovskite films were exposed to ambient air (35% RH), with the Sn^{4+}/Sn^{2+} ratio at the buried interface monitored by XPS. As shown in Fig. S21, the ratio

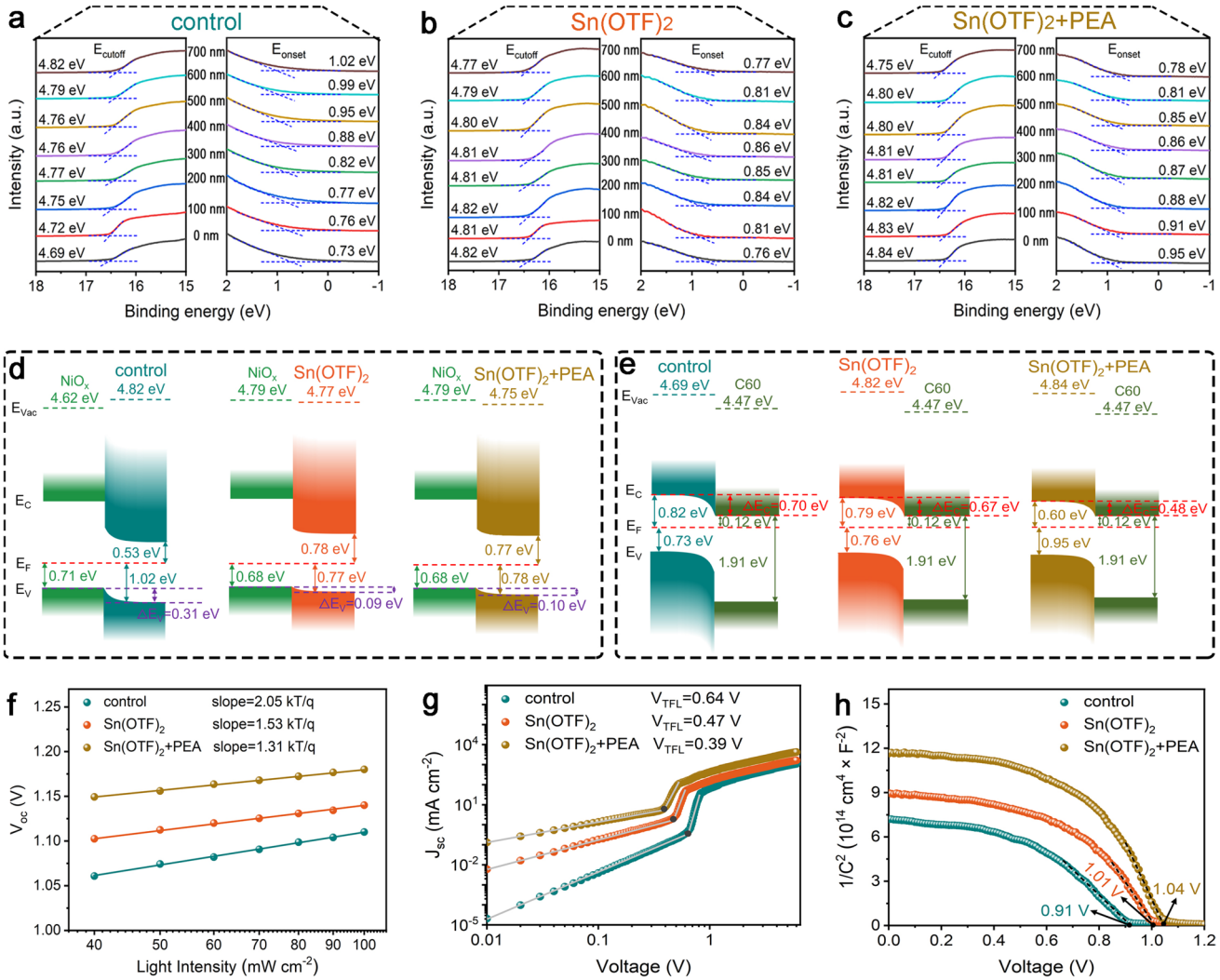

Fig. 5 Depth-profiling UPS spectra of of the **a** control, **b** $Sn(OTF)_2$, and **c** $Sn(OTF)_2$ + PEA films. Energy-level diagrams of the TSP p-i-n PSCs at the **d** NiOx/perovskite and **e** perovskite/C60 interfaces. **f** V_{oc} response under different light intensities of the PSCs. **g** Dark J-V curves for the electron-only devices. **h** Mott–Schottky results for devices based on different films

increased marginally from 14.1% (0 h) to 21.0% (168 h). This slow oxidation kinetics indicates the Pb–Sn interlayer possesses enhanced ambient stability. The mild increase aligns with gradual degradation of unencapsulated films, which is unavoidable under ambient conditions but well-controlled here. Besides, the efficiency of unencapsulated devices was recorded under identical ambient conditions (Fig. S22). The PCE decreased slightly from 25.21% (0 h) to 24.7% (168 h). This minor efficiency reduction was primarily attributed to a slight FF decrease (81.9% to 80.8%), whereas the J_{sc} and V_{oc} remained stable. This confirms that the Pb–Sn mixed perovskite interlayer maintains intact energy-level alignment function (critical for J_{sc} and V_{oc}), and the degradation primarily originates from minor bulk perovskite deterioration rather than interlayer failure. Additionally, similar improvements in long-term and thermal stability under N_2 atmosphere were observed (Fig. 6b, c), which are mainly attributed to improved crystallinity and reduced structural defects that effectively inhibit perovskite crystal degradation. Operational stability testing performed under the ISOS-L-1I protocol (under 1 sun illumination in N_2 atmosphere at room temperature) revealed that the $Sn(OTF)_2$ + PEA device maintained exceptional stability, retaining > 84% of initial performance after 720 h. To estimate the T_{80} lifetime, an established lifetime extrapolation method was employed based on the

 https://doi.org/10.1007/s40820-025-02010-w

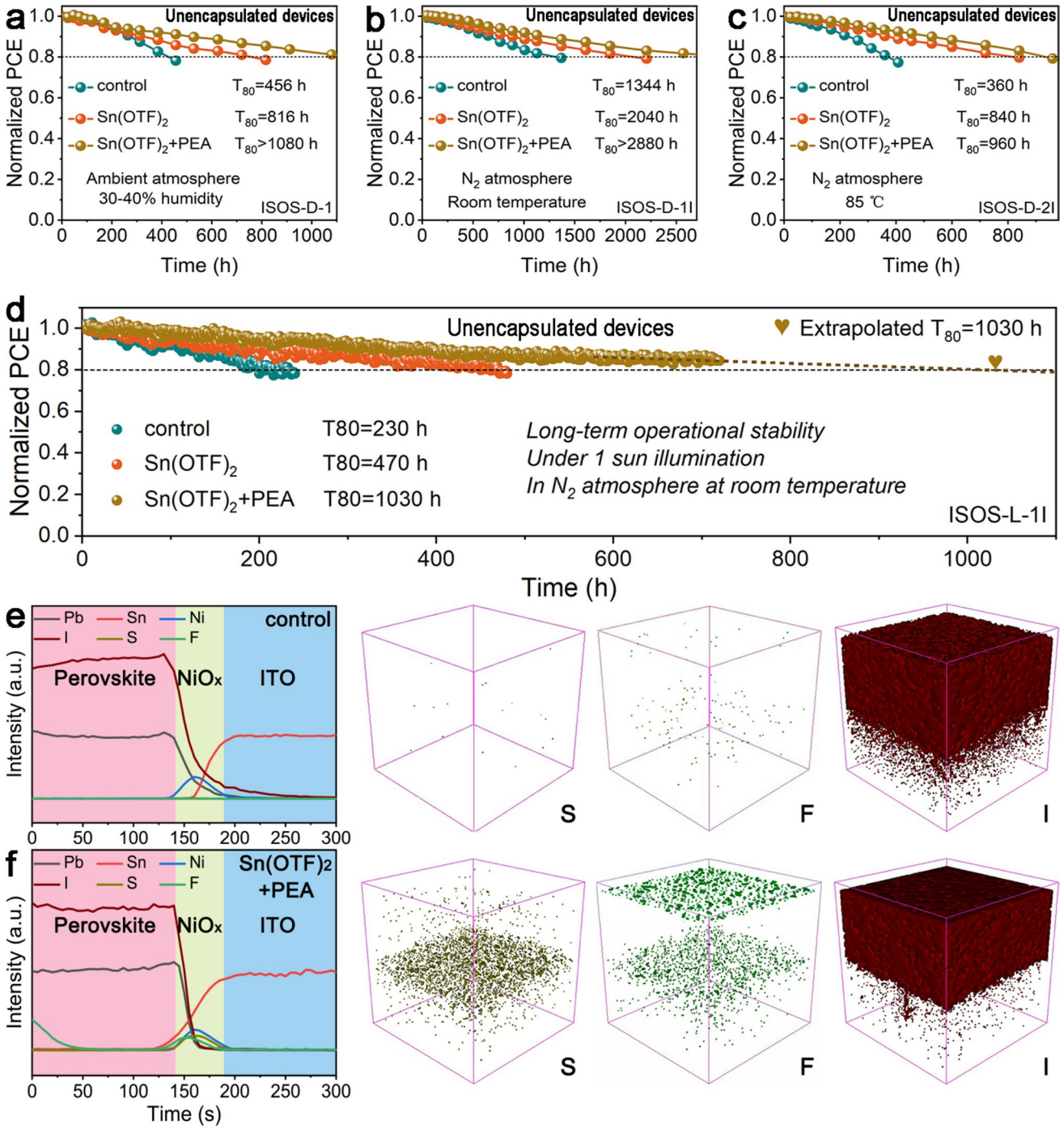

Fig. 6 **a** ISOS-D-1 device stability at RH = 30–40%. **b** ISOS-D-1I device stability in N_2 atmosphere. **c** ISOS-D-2I device stability during storage at 85 °C. **d** ISOS-L-1I device stability under 1 sun illumination. Time-of-flight secondary ion mass spectrometry (TOF–SIMs) depth profiles and corresponding ions distribution of I^-, S^-, and F^- within the **e** control and **f** $Sn(OTF)_2$ + PEA devices

measured data [53]. As shown in Fig. 6d, the extrapolated T_{80} for the $Sn(OTF)_2$ + PEA device was projected to reach 1030 h, indicating a twofold improvement relative to the $Sn(OTF)_2$ device (T_{80} = 470 h) and a fourfold enhancement compared with the control device (T_{80} = 230 h). This significantly enhanced operational stability arises from two key factors: (1) the F-PEA-induced formation of a protective 2D perovskite capping layer, which effectively reduces

residual PbI_2 clusters (known as degradation centers) [23, 54], and (2) strong chemical interactions between –OTF groups and Pb^{2+} (confirmed by DFT calculations, Fig. 2a) that inhibit ion migration toward NiO_x.

To elucidate the suppressed ion migration, time-of-flight secondary ion mass spectrometry (TOF–SIMs) analyses were performed. As shown in Fig. 6e, f, the presence and spatial distribution of S elemental signals in the $Sn(OTF)_2$ + PEA device confirm the successful introduction of the $Sn(OTF)_2$ interlayer at the NiO_x/perovskite interface. Depth-profiling analysis shows that the control device exhibits an increase in I^- intensity and decrease in Pb^{2+} intensity with increasing etching time, further suggesting that the residual PbI_2 is mainly located at the top surface. Furthermore, the $Sn(OTF)_2$ + PEA device reveals a substantial concentration of Sn^{2+} ions within the bottom subsurface region of the perovskite, demonstrating the incorporation of Sn^{2+} ions into the perovskite lattice. Besides, the dual-interface modification in the $Sn(OTF)_2$ + PEA device results in F signals being detected at both top and bottom surfaces of the perovskite. Moreover, the control device shows significantly higher concentrations of Pb^{2+} and I^- ions at the NiO_x/perovskite interface compared to the $Sn(OTF)_2$ + PEA device, indicating that ion migration is effectively suppressed by the $Sn(OTF)_2$ modification. The corresponding three-dimensional I^- ion distribution profiles offer more comprehensive visualization of the suppressed ionic migration within the $Sn(OTF)_2$ + PEA device.

4 Conclusions

In summary, we have demonstrated that TSP perovskite films exhibit vertically gradient distributed residual PbI_2 clusters forming Schottky heterojunctions with perovskite, leading to interfacial energy-level mismatches within the NiO_x-based TSP p-i-n PSCs. To address this issue, a vertical interfacial engineering that relies on the synergistic effect between $Sn(OTF)_2$ and F-PEA has been developed for precise regulation of residual PbI_2 clusters. Specifically, the functional –OTF groups in $Sn(OTF)_2$ exhibit robust interactions with both NiO_x and PbI_2, which demonstrate dual functionality in enhancing the conductivity of NiO_x films while suppressing adverse redox reaction and ion migration from perovskite to the underlying NiO_x layer. Besides, the divalent Sn^{2+} ions spontaneously incorporate into the perovskite lattice, forming a Pb–Sn mixed perovskite interlayer that critically optimizes the energy-level alignment at the NiO_x/perovskite interface. Complementally, F-PEA post-treatment demonstrated efficacy in eliminating residual PbI_2 clusters through the formation of a 2D perovskite capping layer, which significantly improves perovskite/C60 interfacial energy-level alignment while simultaneously passivating surface defects. With this synergistic collaboration between $Sn(OTF)_2$ and F-PEA, the resulting devices deliver a champion PCE of 25.6%, significantly higher than that of $Sn(OTF)_2$-only (23.6%) and control (20.5%) devices.

Acknowledgements This work was financially supported by the National Nature Science Foundation of China (62504130), National Key Research and Development Program of China (2018YFB0704100), the Key university laboratory of highly efficient utilization of solar energy and sustainable development of Guangdong (Y01256331), the Technology Development Project of Henan Province (252102240047). The authors thank the Pico Center at SUSTech CRF which receives support from the Presidential Fund and Development and Reform Commission of Shenzhen Municipality.

Author Contributions Wenhao Zhou, Heng Liu, and Haiyan Li contributed equally to this work. Weihai Zhang, Tingting Shi, Antonio Abate, and Hsing-Lin Wang conceived the idea and directed the project. Wenhao Zhou and Heng Liu designed the experiments and conducted the basic characterization. Haiyan Li helped with the DFT calculations. Hui Li and Xia Zhou helped with the XPS, SEM and NMR characterizations and data analysis. Rouxi Chen and Wenjun Zhang provided valuable suggestions for the manuscript. Weihai Zhang wrote the manuscript. All authors discussed the results and participated in the manuscript preparation.

Declarations

Conflict of interest The authors declare no interest conflict. They have no known competing financial interests or personal relationships that could have appeared to influence the work reported in this paper.

Supplementary Information The online version contains supplementary material available at https://doi.org/10.1007/s40820-025-02010-w.

References

1. J.-P. Correa-Baena, M. Saliba, T. Buonassisi, M. Grätzel, A. Abate et al., Promises and challenges of perovskite solar cells. Science **358**(6364), 739–744 (2017). https://doi.org/10.1126/science.aam6323
2. R. He, X. Huang, M. Chee, F. Hao, P. Dong, Carbon-based perovskite solar cells: from single-junction to modules. Carbon Energy **1**(1), 109–123 (2019). https://doi.org/10.1002/cey2.11
3. National Renewable Energy Laboratory (NREL), Research Cell Efficiency Records, https://www.nrel.gov/pv/cell-efficiency.html (accessed: February 2025).
4. Z. Liu, R. Lin, M. Wei, M. Yin, P. Wu et al., All-perovskite tandem solar cells achieving >29% efficiency with improved (100) orientation in wide-bandgap perovskites. Nat. Mater. **24**(2), 252–259 (2025). https://doi.org/10.1038/s41563-024-02073-x
5. Q. Li, Y. Zheng, H. Wang, X. Liu, M. Lin et al., Graphene-polymer reinforcement of perovskite lattices for durable solar cells. Science **387**(6738), 1069–1077 (2025). https://doi.org/10.1126/science.adu5563
6. Q. Tai, F. Yan, Emerging semitransparent solar cells: materials and device design. Adv. Mater. **29**(34), 1700192 (2017). https://doi.org/10.1002/adma.201700192
7. J. Chen, J. Du, J. Cai, B. Ouyang, Z. Li et al., Lewis base strategy for crystallization control and buried interface passivation on hydrophobic PTAA substrate for efficient tin–lead perovskite and all-perovskite tandem solar cells. ACS Energy Lett. **10**(3), 1117–1128 (2025). https://doi.org/10.1021/acsenergylett.4c03370
8. H. Hyuck, H. Young, P. Kyoung, L. Joon, F. Zhang et al., Chemical oxidization of PTAA enables stable slot-die-coated perovskite solar modules. Joule **9**(4), 101850 (2025). https://doi.org/10.1016/j.joule.2025.101850
9. M.D. Irwin, D.B. Buchholz, A.W. Hains, R.P.H. Chang, T.J. Marks, P-type semiconducting nickel oxide as an efficiency-enhancing anode interfacial layer in polymer bulk-heterojunction solar cells. Proc. Natl. Acad. Sci. U. S. A. **105**(8), 2783–2787 (2008). https://doi.org/10.1073/pnas.0711990105
10. Z. Liu, A. Zhu, F. Cai, L. Tao, Y. Zhou et al., Nickel oxide nanoparticles for efficient hole transport in p-i-n and n-i-p perovskite solar cells. J. Mater. Chem. A **5**(14), 6597–6605 (2017). https://doi.org/10.1039/C7TA01593C
11. H. Zhang, C. Zhao, J. Yao, W.C.H. Choy, Dopant-free NiO_x nanocrystals: a low-cost and stable hole transport material for commercializing perovskite optoelectronics. Angew. Chem. Int. Ed. **62**(24), e202219307 (2023). https://doi.org/10.1002/anie.202219307
12. S. Yu, Z. Xiong, H. Zhou, Q. Zhang, Z. Wang et al., Homogenized NiO_x nanoparticles for improved hole transport in inverted perovskite solar cells. Science **382**(6677), 1399–1404 (2023). https://doi.org/10.1126/science.adj8858
13. S. Liu, J. Li, W. Xiao, R. Chen, Z. Sun et al., Buried interface molecular hybrid for inverted perovskite solar cells. Nature **632**(8025), 536–542 (2024). https://doi.org/10.1038/s41586-024-07723-3
14. J. Fang, D. Lin, G. Xie, S. Li, H. Li et al., Anion exchange promoting non-impurities enables conformable and efficient inverted perovskite solar cells. Energy Environ. Sci. **17**(20), 7829–7837 (2024). https://doi.org/10.1039/D4EE02718C
15. P. Chen, Y. Xiao, L. Li, L. Zhao, M. Yu, S. Li, J. Hu, B. Liu, Y. Yang, D. Luo, C.-H. Hou, X. Guo, J.-J. Shyue, Z.-H. Lu, Q. Gong, H.J. Snaith, R. Zhu, Efficient inverted perovskite solar cells *via* improved sequential deposition. Adv. Mater. **35**(5), 2206345 (2023). https://doi.org/10.1002/adma.202206345
16. H. Bao, S. Wang, H. Liu, X. Li, Columnar liquid crystal enables *in situ* dispersing of excess PbI_2 crystals for efficient and stable perovskite solar cells. Adv. Energy Mater. **14**(8), 2303166 (2024). https://doi.org/10.1002/aenm.202303166
17. J. Holovský, A.P. Amalathas, L. Landová, B. Dzurňák, B. Conrad et al., Lead halide residue as a source of light-induced reversible defects in hybrid perovskite layers and solar cells. ACS Energy Lett. **4**(12), 3011–3017 (2019). https://doi.org/10.1021/acsenergylett.9b02080
18. H. Liu, J. Wang, Y. Qu, H. Zhou, Y. Xia et al., Defect management and ion infiltration barrier enable high-performance perovskite solar cells. ACS Energy Lett. **9**(6), 2790–2799 (2024). https://doi.org/10.1021/acsenergylett.4c00059
19. G. Tong, D.-Y. Son, L.K. Ono, Y. Liu, Y. Hu et al., Scalable fabrication of >90 Cm2 perovskite solar modules with >1000 h operational stability based on the intermediate phase strategy. Adv. Energy Mater. **11**(10), 2003712 (2021). https://doi.org/10.1002/aenm.202003712
20. C. Deng, J. Wu, Y. Yang, Y. Du, R. Li et al., Modulating residual lead iodide *via* functionalized buried interface for efficient and stable perovskite solar cells. ACS Energy Lett. **8**(1), 666–676 (2023). https://doi.org/10.1021/acsenergylett.2c02378
21. C. Wang, D. Qu, R. Han, X. Zhang, C. Shang et al., Dipole molecule-mediated modulating residual PbI_2 clusters in two-step-processing inverted perovskite photovoltaics. Nano Lett. **24**(49), 15912–15920 (2024). https://doi.org/10.1021/acs.nanolett.4c05022
22. J. Zhang, X. Ji, X. Wang, L. Zhang, L. Bi et al., Efficient and stable inverted perovskite solar modules enabled by solid-liquid two-step film formation. Nano-Micro Lett. **16**(1), 190 (2024). https://doi.org/10.1007/s40820-024-01408-2
23. Y. Gao, F. Ren, D. Sun, S. Li, G. Zheng et al., Elimination of unstable residual lead iodide near the buried interface for the stability improvement of perovskite solar cells. Energy

Environ. Sci. **16**(5), 2295–2303 (2023). https://doi.org/10.1039/D3EE00293D

24. D. Qu, C. Shang, X. Yang, C. Wang, B. Zhou et al., Phase homogeneity mediated charge-carrier balance in two-step-method halide perovskite photovoltaics. Energy Environ. Sci. **18**(3), 1310–1319 (2025). https://doi.org/10.1039/D4EE04419C
25. Y. Zhao, F. Ma, Z. Qu, S. Yu, T. Shen et al., Inactive $(PbI_2)_2RbCl$ stabilizes perovskite films for efficient solar cells. Science **377**(6605), 531–534 (2022). https://doi.org/10.1126/science.abp8873
26. M. Tao, Y. Wang, K. Zhang, Z. Song, Y. Lan et al., Molecule-triggered strain regulation and interfacial passivation for efficient inverted perovskite solar cells. Joule **8**(11), 3142–3152 (2024). https://doi.org/10.1016/j.joule.2024.08.003
27. J. He, W. Sheng, J. Yang, Y. Zhong, Y. Su et al., Omnidirectional diffusion of organic amine salts assisted by ordered arrays in porous lead iodide for two-step deposited large-area perovskite solar cells. Energy Environ. Sci. **16**(2), 629–640 (2023). https://doi.org/10.1039/D2EE03418B
28. H. Chen, H. Yan, Y. Cai, Effects of defect on work function and energy alignment of PbI_2: implications for solar cell applications. Chem. Mater. **34**(3), 1020–1029 (2022). https://doi.org/10.1021/acs.chemmater.1c03238
29. K. Chen, Q. Hu, T. Liu, L. Zhao, D. Luo, J. Wu, Y. Zhang, W. Zhang, F. Liu, T.P. Russell, R. Zhu, Q. Gong, Charge-carrier balance for highly efficient inverted planar heterojunction perovskite solar cells. Adv. Mater. **28**(48), 10718–10724 (2016). https://doi.org/10.1002/adma.201604048
30. W. Zhang, H. Liu, T. Huang, L. Kang, J. Ge, H. Li, X. Zhou, T. Shi, H.-L. Wang, Oriented molecular dipole-enabled modulation of NiOx/perovskite interface for Pb-Sn mixed inorganic perovskite solar cells. Adv. Mater. **37**(8), 2414125 (2025). https://doi.org/10.1002/adma.202414125
31. F. Wang, T. Wang, Y. Sun, X. Liang, G. Yang et al., Two-step perovskite solar cells with > 25% efficiency: unveiling the hidden bottom surface of perovskite layer. Adv. Mater. **36**(31), 2401476 (2024). https://doi.org/10.1002/adma.202401476
32. R. Chen, Y. Wang, S. Nie, H. Shen, Y. Hui et al., Sulfonate-assisted surface iodide management for high-performance perovskite solar cells and modules. J. Am. Chem. Soc. **143**(28), 10624–10632 (2021). https://doi.org/10.1021/jacs.1c03419
33. Y. Wang, R. Lin, C. Liu, X. Wang, C. Chosy et al., Homogenized contact in all-perovskite tandems using tailored 2D perovskite. Nature **635**(8040), 867–873 (2024). https://doi.org/10.1038/s41586-024-08158-6
34. X. Ren, J. Wang, Y. Lin, Y. Wang, H. Xie et al., Mobile iodides capture for highly photolysis- and reverse-bias-stable perovskite solar cells. Nat. Mater. **23**(6), 810–817 (2024). https://doi.org/10.1038/s41563-024-01876-2
35. X. Feng, B. Liu, Y. Peng, C. Gu, X. Bai et al., Restricting the formation of Pb–Pb dimer *via* surface Pb site passivation for enhancing the light stability of perovskite. Small **18**(23), 2201831 (2022). https://doi.org/10.1002/smll.202201831
36. L. Zhao, Z. Shi, Y. Zhou, X. Wang, Y. Xian et al., Surface-defect-passivation-enabled near-unity charge collection efficiency in bromide-based perovskite gamma-ray spectrum devices. Nat. Photon. **18**(3), 250–257 (2024). https://doi.org/10.1038/s41566-023-01356-0
37. J. Zhang, J. Yang, R. Dai, W. Sheng, Y. Su, Y. Zhong, X. Li, L. Tan, Y. Chen, Elimination of interfacial lattice mismatch and detrimental reaction by self-assembled layer dual-passivation for efficient and stable inverted perovskite solar cells. Adv. Energy Mater. **12**(18), 2103674 (2022). https://doi.org/10.1002/aenm.202103674
38. D. Yang, R. Yang, K. Wang, C. Wu, X. Zhu et al., High efficiency planar-type perovskite solar cells with negligible hysteresis using EDTA-complexed SnO_2. Nat. Commun. **9**(1), 3239 (2018). https://doi.org/10.1038/s41467-018-05760-x
39. P.A. Fernández Garrillo, B. Grévin, N. Chevalier, Ł Borowik, Calibrated work function mapping by Kelvin probe force microscopy. Rev. Sci. Instrum. **89**(4), 043702 (2018). https://doi.org/10.1063/1.5007619
40. W. Melitz, J. Shen, A.C. Kummel, S. Lee, Kelvin probe force microscopy and its application. Surf. Sci. Rep. **66**(1), 1–27 (2011). https://doi.org/10.1016/j.surfrep.2010.10.001
41. Q. Wang, J. Zhu, Y. Zhao, Y. Chang, N. Hao, Z. Xin, Q. Zhang, C. Chen, H. Huang, Q. Tang, Cross-layer all-interface defect passivation with pre-buried additive toward efficient all-inorganic perovskite solar cells. Carbon Energy **6**(9), e566 (2024). https://doi.org/10.1002/cey2.566
42. Y. Zhou, T. Guo, J. Jin, Z. Zhu, Y. Li et al., Defect-less formamidinium Sn–Pb perovskite grown on a fluorinated substrate with top-down crystallization control for efficient and stable photovoltaics. Energy Environ. Sci. **17**(8), 2845–2855 (2024). https://doi.org/10.1039/D3EE04343F
43. W. Zhang, J. Xiong, J. Li, W.A. Daoud, Seed-assisted growth for low-temperature-processed all-inorganic CsPbIBr2 solar cells with efficiency over 10%. Small **16**(24), 2001535 (2020). https://doi.org/10.1002/smll.202001535
44. A. Goyal, S. McKechnie, D. Pashov, W. Tumas, M. van Schilfgaarde et al., Origin of pronounced nonlinear band gap behavior in lead–tin hybrid perovskite alloys. Chem. Mater. **30**(11), 3920–3928 (2018). https://doi.org/10.1021/acs.chemmater.8b01695
45. W. Zhang, H. Liu, X. Qi, Y. Yu, Y. Zhou et al., Oxalate pushes efficiency of $CsPb_{0.7}Sn_{0.3}IBr_2$ based all-inorganic perovskite solar cells to over 14%. Adv. Sci. **9**(11), 2106054 (2022). https://doi.org/10.1002/advs.202106054
46. X. Zhang, Y. Luo, X. Wang, K. Zhao, P. Shi, Y. Tian, J. Xu, L. Yao, J. Sun, Q. Liu, W. Fan, R. Wang, J. Xue, Locking surface dimensionality for endurable interface in perovskite photovoltaics. Carbon Energy **7**(4), e718 (2025). https://doi.org/10.1002/cey2.718
47. W. Zhang, Y. Cai, H. Liu, Y. Xia, J. Cui, Y. Shi, R. Chen, T. Shi, H.-L. Wang, Organic-free and lead-free perovskite solar cells with efficiency over 11%. Adv. Energy Mater. **12**(42), 2202491 (2022). https://doi.org/10.1002/aenm.202202491

 https://doi.org/10.1007/s40820-025-02010-w

48. W. Zhang, H. Liu, Y. Qu, J. Cui, W. Zhang, T. Shi, H.L. Wang, B-site co-doping coupled with additive passivation pushes the efficiency of Pb–Sn mixed inorganic perovskite solar cells to over 17%. Adv. Mater. **36**(14), 2309193 (2024). https://doi.org/10.1002/adma.202309193
49. V.M. Le Corre, E.A. Duijnstee, O. El Tambouli, J.M. Ball, H.J. Snaith et al., Revealing charge carrier mobility and defect densities in metal halide perovskites *via* space-charge-limited current measurements. ACS Energy Lett. **6**(3), 1087–1094 (2021). https://doi.org/10.1021/acsenergylett.0c02599
50. C. Liu, L. Ma, P. Zhao, L. Yuan, F. Li, Z. Fang, Q. Chang, N. Jia, P. Guo, F. Guo, Z. Liu, R. Chen, H. Wang, Peptide-based ammonium halide with inhibited deprotonation enabling effective interfacial engineering for highly efficient and stable FAPbI3 perovskite solar cells. Adv. Funct. Mater. **34**(40), 2405735 (2024). https://doi.org/10.1002/adfm.202405735
51. O. Almora, C. Aranda, E. Mas-Marzá, G. Garcia-Belmonte, On mott-schottky analysis interpretation of capacitance measurements in organometal perovskite solar cells. Appl. Phys. Lett. **109**(17), 173903 (2016). https://doi.org/10.1063/1.4966127
52. E.L. Lim, A. Hagfeldt, D. Bi, Toward highly efficient and stable Sn^{2+} and mixed Pb^{2+}/Sn^{2+} based halide perovskite solar cells through device engineering. Energy Environ. Sci. **14**(6), 3256–3300 (2021). https://doi.org/10.1039/D0EE03368E
53. K. Zhao, Q. Liu, L. Yao, C. Değer, J. Shen et al., Peri-fused polyaromatic molecular contacts for perovskite solar cells. Nature **632**(8024), 301–306 (2024). https://doi.org/10.1038/s41586-024-07712-6
54. Y. Gao, H. Raza, Z. Zhang, W. Chen, Z. Liu, Rethinking the role of excess/residual lead iodide in perovskite solar cells. Adv. Funct. Mater. **33**(26), 2215171 (2023). https://doi.org/10.1002/adfm.202215171